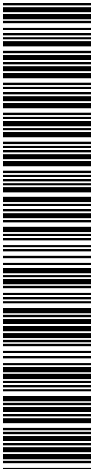


Photoproduction of $D^{*\pm}$ Mesons in Electron-Proton Collisions at HERA

H1 Collaboration

Abstract

At the electron-proton collider HERA the inclusive $D^{*\pm}$ meson photoproduction cross section has been measured with the H1 detector in two different, but partly overlapping, kinematical regions. For the first, where $\langle W_{\gamma p} \rangle \approx 200$ GeV and $Q^2 < 0.01$ GeV², the result is $\sigma(\gamma p \rightarrow c\bar{c}X) = (13.2 \pm 2.2^{+2.1}_{-1.7} {}^{+9.9}_{-4.8}) \mu\text{b}$. The second measurement for $Q^2 < 4$ GeV² yields $\sigma(\gamma p \rightarrow c\bar{c}X) = (9.3 \pm 2.1^{+1.9}_{-1.8} {}^{+6.9}_{-3.2}) \mu\text{b}$ at $\langle W_{\gamma p} \rangle \approx 142$ GeV and $\sigma(\gamma p \rightarrow c\bar{c}X) = (20.6 \pm 5.5^{+4.3}_{-3.9} {}^{+15.4}_{-7.2}) \mu\text{b}$ at $\langle W_{\gamma p} \rangle \approx 230$ GeV, respectively. The third error accounts for an additional uncertainty due to the proton and photon parton density parametrizations. Differential cross sections are presented as a function of the $D^{*\pm}$ transverse momentum and rapidity. The results compare reasonably well with next-to-leading order QCD calculations. Evidence for diffractive photoproduction of charm quarks is presented.



S. Aid¹⁴, V. Andreev²⁶, B. Andrieu²⁹, R.-D. Appuhn¹², M. Arpagaus³⁷, A. Babaev²⁵, J. Bähr³⁶, J. Bán¹⁸,
 Y. Ban²⁸, P. Baranov²⁶, E. Barrelet³⁰, R. Barschke¹², W. Bartel¹², M. Barth⁵, U. Bassler³⁰, H.P. Beck³⁸,
 H.-J. Behrend¹², A. Belousov²⁶, Ch. Berger¹, G. Bernardi³⁰, R. Bernet³⁷, G. Bertrand-Coremans⁵, M. Be-
 sangon¹⁰, R. Beyer¹², P. Biddulph²³, P. Bispham²³, J.C. Bizot²⁸, V. Blobel¹⁴, K. Borrás⁹, F. Botterweck⁵,
 V. Boudry²⁹, A. Braemer¹⁵, W. Braunschweig¹, V. Brisson²⁸, D. Bruncko¹⁸, C. Brune¹⁶, R. Buchholz¹²,
 L. Büngener¹⁴, J. Bürger¹², F.W. Büsler¹⁴, A. Buniatian^{12,39}, S. Burke¹⁹, M.J. Burton²³, G. Buschhorn²⁷,
 A.J. Campbell¹², T. Carli²⁷, M. Charlet¹², D. Clarke⁶, A.B. Clegg¹⁹, B. Clerbaux⁵, S. Cocks²⁰,
 J.G. Contreras⁹, C. Cormack²⁰, J.A. Coughlan⁶, A. Courau²⁸, M.-C. Cousinou²⁴, G. Cozzika¹⁰,
 L. Criegee¹², D.G. Cussans⁶, J. Cvach³¹, S. Dagoret³⁰, J.B. Dainton²⁰, W.D. Dau¹⁷, K. Daum³⁵,
 M. David¹⁰, C.L. Davis¹⁹, B. Delcourt²⁸, A. De Roeck¹², E.A. De Wolf⁵, M. Dirkmann⁹, P. Dixon¹⁹,
 P. Di Nezza³³, W. Dlugosz⁸, C. Dollfus³⁸, J.D. Dowell⁴, H.B. Dreis², A. Droutskoi²⁵, D. Düllmann¹⁴,
 O. Dünger¹⁴, H. Duhm¹³, J. Ebert³⁵, T.R. Ebert²⁰, G. Eckerlin¹², V. Efremenko²⁵, S. Egli³⁸,
 R. Eichler³⁷, F. Eisele¹⁵, E. Eisenhandler²¹, R.J. Ellison²³, E. Elsen¹², M. Erdmann¹⁵, W. Erdmann³⁷,
 E. Evrard⁵, A.B. Fahr¹⁴, L. Favart²⁸, A. Fedotov²⁵, D. Feeken¹⁴, R. Felst¹², J. Feltesse¹⁰, J. Ferencei¹⁸,
 F. Ferrarotto³³, K. Flamm¹², M. Fleischer⁹, M. Fliesser²⁷, G. Flügge², A. Fomenko²⁶, B. Fominykh²⁵,
 J. Formánek³², J.M. Foster²³, G. Franke¹², E. Fretwurst¹³, E. Gabathuler²⁰, K. Gabathuler³⁴,
 F. Gaede²⁷, J. Garvey⁴, J. Gayler¹², M. Gebauer³⁶, A. Gellrich¹², H. Genzel¹, R. Gerhards¹²,
 A. Glazov³⁶, U. Goerlach¹², L. Goerlich⁷, N. Gogitidze²⁶, M. Goldberg³⁰, D. Goldner⁹, K. Golec-
 Biernat⁷, B. Gonzalez-Pineiro³⁰, I. Gorelov²⁵, C. Grab³⁷, H. Grässler², R. Grässler², T. Greenshaw²⁰,
 R.K. Griffiths²¹, G. Grindhammer²⁷, A. Gruber²⁷, C. Gruber¹⁷, J. Haack³⁶, T. Hadig¹, D. Haidt¹²,
 L. Hajduk⁷, M. Hampel¹, W.J. Haynes⁶, G. Heinzelmann¹⁴, R.C.W. Henderson¹⁹, H. Henschel³⁶,
 I. Herynek³¹, M.F. Hess²⁷, W. Hildesheim¹², K.H. Hiller³⁶, C.D. Hilton²³, J. Hladký³¹, K.C. Hoeger²³,
 M. Höppner⁹, D. Hoffmann¹², T. Holtom²⁰, R. Horisberger³⁴, V.L. Hudgson⁴, M. Hütte⁹, H. Hufnagel¹⁵,
 M. Ibbotson²³, H. Itterbeck¹, A. Jacholkowska²⁸, C. Jacobsson²², M. Jaffre²⁸, J. Janoth¹⁶, T. Jansen¹²,
 L. Jönsson²², K. Johannsen¹⁴, D.P. Johnson⁵, L. Johnson¹⁹, H. Jung¹⁰, P.I.P. Kalmus²¹, M. Kander¹²,
 D. Kant²¹, R. Kaschowitz², U. Kathage¹⁷, J. Katzy¹⁵, H.H. Kaufmann³⁶, O. Kaufmann¹⁵, S. Kazarian¹²,
 I.R. Kenyon⁴, S. Kermiche²⁴, C. Keuker¹, C. Kiesling²⁷, M. Klein³⁶, C. Kleinwort¹², G. Knies¹²,
 T. Köhler¹, J.H. Köhne²⁷, H. Kolanoski³, F. Kole⁸, S.D. Kolya²³, V. Korbelt¹², M. Korn⁹, P. Kostka³⁶,
 S.K. Kotelnikov²⁶, T. Krämerländer⁹, M.W. Krasny^{7,30}, H. Krehbiel¹², D. Krücker², U. Krüger¹²,
 U. Krüner-Marquis¹², H. Küster²², M. Kuhlen²⁷, T. Kurča³⁶, J. Kurzhöfer⁹, D. Lacour³⁰, B. Laforge¹⁰,
 R. Lander⁸, M.P.J. Landon²¹, W. Lange³⁶, U. Langenegger³⁷, J.-F. Laporte¹⁰, A. Lebedev²⁶, F. Lehner¹²,
 C. Leverenz¹², S. Levonian²⁹, Ch. Ley², G. Lindström¹³, M. Lindstroem²², J. Link⁸, F. Linsel¹²,
 J. Lipinski¹⁴, B. List¹², G. Lobo²⁸, H. Lohmander²², J.W. Lomas²³, G.C. Lopez¹³, V. Lubimov²⁵,
 D. Lüke^{9,12}, N. Magnussen³⁵, E. Malinovski²⁶, S. Mani⁸, R. Maraček¹⁸, P. Marage⁵, J. Marks²⁴,
 R. Marshall²³, J. Martens³⁵, G. Martin¹⁴, R. Martin²⁰, H.-U. Martyn¹, J. Martyniak⁷, T. Mavroidis²¹,
 S.J. Maxfield²⁰, S.J. McMahon²⁰, A. Mehta⁶, K. Meier¹⁶, T. Merz³⁶, A. Meyer¹², A. Meyer¹⁴,
 H. Meyer³⁵, J. Meyer¹², P.-O. Meyer², A. Migliori²⁹, S. Mikocki⁷, D. Milstead²⁰, J. Moeck²⁷,
 F. Moreau²⁹, J.V. Morris⁶, E. Mroczko⁷, D. Müller³⁸, G. Müller¹², K. Müller¹², P. Murin¹⁸,
 V. Nagovizin²⁵, R. Nahnauer³⁶, B. Naroska¹⁴, Th. Naumann³⁶, P.R. Newman⁴, D. Newton¹⁹,
 D. Neyret³⁰, H.K. Nguyen³⁰, T.C. Nicholls⁴, F. Niebergall¹⁴, C. Niebuhr¹², Ch. Niedzballa¹, H. Niggli³⁷,
 R. Nisius¹, G. Nowak⁷, G.W. Noyes⁶, M. Nyberg-Werther²², M. Oakden²⁰, H. Oberlack²⁷, U. Obrock⁹,
 J.E. Olsson¹², D. Ozerov²⁵, P. Palmes², E. Panaro¹², A. Panitch⁵, C. Pascaud²⁸, G.D. Patel²⁰,
 H. Pawletta², E. Poppel³⁶, E. Perez¹⁰, J.P. Phillips²⁰, A. Pieuchot²⁴, D. Pitzl³⁷, G. Pope⁸, S. Prell¹²,
 R. Prosi¹², K. Rabbertz¹, G. Rädelt¹², F. Raupach¹, P. Reimer³¹, S. Reinshagen¹², H. Rick⁹,
 V. Riech¹³, J. Riedlberger³⁷, F. Riepenhausen², S. Riess¹⁴, E. Rizvi²¹, S.M. Robertson⁴, P. Robmann³⁸,
 H.E. Roloff^{36,1}, R. Roosen⁵, K. Rosenbauer¹, A. Rostovtsev²⁵, F. Rouse⁸, C. Royon¹⁰, K. Rüter²⁷,
 S. Rusakov²⁶, K. Rybicki⁷, N. Sahlmann², D.P.C. Sankey⁶, P. Schacht²⁷, S. Schiek¹⁴, S. Schleich¹⁶,
 P. Schleper¹⁵, W. von Schlippe²¹, D. Schmidt³⁵, G. Schmidt¹⁴, A. Schöning¹², V. Schröder¹²,
 E. Schuhmann²⁷, B. Schwab¹⁵, F. Sefkow³⁸, M. Seidel¹³, R. Sell¹², A. Semenov²⁵, V. Shekelyan¹²,
 I. Sheviakov²⁶, L.N. Shtarkov²⁶, G. Siegmund¹⁷, U. Siewert¹⁷, Y. Sirois²⁹, I.O. Skillicorn¹¹, P. Smirnov²⁶,
 J.R. Smith⁸, V. Solochenko²⁵, Y. Soloviev²⁶, A. Specka²⁹, J. Spiekermann⁹, S. Spielman²⁹, H. Spitzer¹⁴,
 F. Squinabol²⁸, R. Starosta¹, M. Steenbock¹⁴, P. Steffen¹², R. Steinberg², H. Steiner^{12,40}, B. Stella³³,
 A. Stellberger¹⁶, J. Stier¹², J. Stiewe¹⁶, U. Stöcklein³⁶, K. Stolze³⁶, U. Straumann¹⁵, W. Struczinski²,
 J.P. Sutton⁴, S. Tapprogge¹⁶, M. Taševský³², V. Tchernyshov²⁵, S. Tchetchelnitski²⁵, J. Theissen²,
 C. Thiebaut²⁹, G. Thompson²¹, P. Truöl³⁸, J. Turnau⁷, J. Tutas¹⁵, P. Uelkes², A. Usik²⁶, S. Valkár³²,
 A. Valkárova³², C. Vallée²⁴, D. Vandenplas²⁹, P. Van Esch⁵, P. Van Mechelen⁵, Y. Vazdik²⁶,

P. Verrecchia¹⁰, G. Villet¹⁰, K. Wacker⁹, A. Wagener², M. Wagener³⁴, A. Walther⁹, B. Waugh²³, G. Weber¹⁴, M. Weber¹², D. Wegener⁹, A. Wegner²⁷, T. Wengler¹⁵, M. Werner¹⁵, L.R. West⁴, T. Wilksen¹², S. Willard⁸, M. Winde³⁶, G.-G. Winter¹², C. Wittek¹⁴, E. Wünsch¹², J. Žáček³², D. Zarbock¹³, Z. Zhang²⁸, A. Zhokin²⁵, F. Zomer²⁸, J. Zsembery¹⁰, K. Zuber¹⁶, and M. zurNedden³⁸

- ¹ I. Physikalisches Institut der RWTH, Aachen, Germany^a
² III. Physikalisches Institut der RWTH, Aachen, Germany^a
³ Institut für Physik, Humboldt-Universität, Berlin, Germany^a
⁴ School of Physics and Space Research, University of Birmingham, Birmingham, UK^b
⁵ Inter-University Institute for High Energies ULB-VUB, Brussels; Universitaire Instelling Antwerpen, Wilrijk; Belgium^c
⁶ Rutherford Appleton Laboratory, Chilton, Didcot, UK^b
⁷ Institute for Nuclear Physics, Cracow, Poland^d
⁸ Physics Department and IIRPA, University of California, Davis, California, USA^e
⁹ Institut für Physik, Universität Dortmund, Dortmund, Germany^a
¹⁰ CEA, DSM/DAPNIA, CE-Saclay, Gif-sur-Yvette, France
¹¹ Department of Physics and Astronomy, University of Glasgow, Glasgow, UK^b
¹² DESY, Hamburg, Germany^a
¹³ I. Institut für Experimentalphysik, Universität Hamburg, Hamburg, Germany^a
¹⁴ II. Institut für Experimentalphysik, Universität Hamburg, Hamburg, Germany^a
¹⁵ Physikalisches Institut, Universität Heidelberg, Heidelberg, Germany^a
¹⁶ Institut für Hochenergiephysik, Universität Heidelberg, Heidelberg, Germany^a
¹⁷ Institut für Reine und Angewandte Kernphysik, Universität Kiel, Kiel, Germany^a
¹⁸ Institute of Experimental Physics, Slovak Academy of Sciences, Košice, Slovak Republic^f
¹⁹ School of Physics and Chemistry, University of Lancaster, Lancaster, UK^b
²⁰ Department of Physics, University of Liverpool, Liverpool, UK^b
²¹ Queen Mary and Westfield College, London, UK^b
²² Physics Department, University of Lund, Lund, Sweden^g
²³ Physics Department, University of Manchester, Manchester, UK^b
²⁴ CPPM, Université d'Aix-Marseille II, IN2P3-CNRS, Marseille, France
²⁵ Institute for Theoretical and Experimental Physics, Moscow, Russia
²⁶ Lebedev Physical Institute, Moscow, Russia^f
²⁷ Max-Planck-Institut für Physik, München, Germany^a
²⁸ LAL, Université de Paris-Sud, IN2P3-CNRS, Orsay, France
²⁹ LPNHE, Ecole Polytechnique, IN2P3-CNRS, Palaiseau, France
³⁰ LPNHE, Universités Paris VI and VII, IN2P3-CNRS, Paris, France
³¹ Institute of Physics, Czech Academy of Sciences, Praha, Czech Republic^{f,h}
³² Nuclear Center, Charles University, Praha, Czech Republic^{f,h}
³³ INFN Roma and Dipartimento di Fisica, Università "La Sapienza", Roma, Italy
³⁴ Paul Scherrer Institut, Villigen, Switzerland
³⁵ Fachbereich Physik, Bergische Universität Gesamthochschule Wuppertal, Wuppertal, Germany^a
³⁶ DESY, Institut für Hochenergiephysik, Zeuthen, Germany^a
³⁷ Institut für Teilchenphysik, ETH, Zürich, Switzerlandⁱ
³⁸ Physik-Institut der Universität Zürich, Zürich, Switzerlandⁱ
³⁹ Visitor from Yerevan Phys. Inst., Armenia
⁴⁰ On leave from LBL, Berkeley, USA

† Deceased

^a Supported by the Bundesministerium für Bildung, Wissenschaft, Forschung und Technologie, FRG, under contract numbers 6AC17P, 6AC47P, 6DO57I, 6HH17P, 6HH27I, 6HD17I, 6HD27I, 6KI17P, 6MP17I, and 6WT87P

^b Supported by the UK Particle Physics and Astronomy Research Council, and formerly by the UK Science and Engineering Research Council

^c Supported by FNRS-NFWO, IISN-IKW

^d Supported by the Polish State Committee for Scientific Research, grant nos. 115/E-743/SPUB/P03/109/95 and 2 P03B 244 08p01, and Stiftung für Deutsch-Polnische Zusammenarbeit, project no.506/92

^e Supported in part by USDOE grant DE F603 91ER40674

^f Supported by the Deutsche Forschungsgemeinschaft

^g Supported by the Swedish Natural Science Research Council

^h Supported by GA ČR, grant no. 202/93/2423, GA AV ČR, grant no. 19095 and GA UK, grant no. 342

ⁱ Supported by the Swiss National Science Foundation

1 Introduction

The study of heavy quark production in lepton-proton scattering provides an important testing ground for the standard model [1]. At the electron-proton collider HERA, heavy quarks are produced, according to QCD, by direct and hadronic (resolved) photon processes. The direct *photon gluon fusion* process $\gamma g \rightarrow c\bar{c}$, where a photon emitted by the electron and a gluon from the proton generate a $c\bar{c}$ pair is expected to dominate. The major contribution is due to the exchange of an almost real photon (*photoproduction*), where the negative squared four-momentum transfer carried by the photon is $Q^2 \approx 0$. The scattered electron is either lost in the beampipe or detected at small angles with respect to the electron beam direction. The fraction of $c\bar{c}$ events where the scattered electron is seen in the main detector (*Deep Inelastic Scattering, DIS, $Q^2 > 4 \text{ GeV}^2$*) is at least one order of magnitude smaller [2]. Measurements at HERA can be considered as a continuation of fixed-target photoproduction experiments [3], but at about one order of magnitude higher centre-of-mass (CM) energies, $W_{\gamma p} \sim \mathcal{O}(200) \text{ GeV}$.

In the *Weizsäcker-Williams Approximation* (WWA) [4], the electroproduction cross section σ_{ep} is expressed as a convolution of the flux of photons emitted by the electron, $f_{\gamma/e}$, with the photoproduction cross section

$$\sigma_{ep} = \sigma(ep \rightarrow ec\bar{c}X) = \int dy f_{\gamma/e}(y) \cdot \sigma(\gamma p \rightarrow c\bar{c}X), \quad (1)$$

where y represents the fraction of the electron energy transferred to the photon in the proton rest frame. For the *direct* photoproduction process, the cross section $\sigma_{\gamma p}$, in turn, is assumed in leading order to factorize into the photon gluon fusion cross section and the gluon density in the proton

$$\sigma_{\gamma p} = \sigma(\gamma p \rightarrow c\bar{c}X) = \int dx_g x_g g(x_g, \mu^2) \cdot \sigma(\gamma g \rightarrow c\bar{c}). \quad (2)$$

Here x_g denotes the momentum fraction of the proton carried by the gluon and μ the factorization scale. Estimates of the cross sections depend on the behaviour of the gluon density distribution g of the proton at small x_g , on the QCD renormalization scale, on the factorization scale, and on the heavy quark mass m_c [5].

Next-to-leading order (NLO) corrections to the parton cross section [5, 6] are found to be substantial, but are reduced by experimental selection criteria, which limit the acceptance to the central rapidity range in the γp CM system at large transverse momenta [5].

Charm photoproduction can also proceed via the hadronic component of the photon (*resolved photon processes*), where a parton inside the photon scatters off a parton inside the proton, *e.g.* $gg \rightarrow c\bar{c}$. This process known to dominate light quark production is expected to contribute much less to the production of charmed quark pairs [5]. However, the production cross section still depends strongly on the parton density function of the photon [7]. Other mechanisms, as for example the production of charm in the fragmentation process, which is suppressed by the mass of the charm quark, or the production from the intrinsic charm content of the nucleon [8], are believed to be small. These processes, as well as any possible intrinsic charm component of the photon, are neglected in the present analysis.

Heavy quark production offers in principle the possibility of probing the gluon distribution in the proton and the photon either indirectly, by measurement of the total

photoproduction cross section or of differential distributions, or directly, by the explicit reconstruction of x_g . Measurements of the first kind are described here. A similar measurement of $\sigma_{\gamma p}$ has also been reported by the ZEUS Collaboration [9].

The analysis makes use of the D^* -tagging [10], *i.e.* of the tight kinematical conditions in the decay¹ $D^{*+} \rightarrow D^0 \pi^+$, where the D^0 mesons are reconstructed in the decay channel $D^0 \rightarrow K^- \pi^+$. A better resolution is achieved in the distribution of the mass difference

$$\Delta M = M(D^0 \pi^+) - M(D^0) \quad (3)$$

than in the D^{*+} mass distribution itself, whose width is dominated by the momentum resolution of the detector.

The contribution of D^{*+} mesons, originating from decays of b flavoured hadrons is neglected, because of the expected small b production cross section at HERA ($\mathcal{O}(5 \text{ nb})$ [11]). D^{*+} mesons from decays of higher-mass charm states (*e.g.* D^{**}) are not separated.

Recently, much interest has been focused on a subclass of electroproduction events in which there is no hadronic energy flow in an interval of pseudorapidity, $\eta = -\ln \tan(\theta/2)$, adjacent to the proton beam direction. These diffractive processes are interpreted as an exchange of a colour-less object with the quantum numbers of the vacuum. The study of charm production in these processes is expected to provide information on the partonic structure of diffractive exchange.

2 Analysis

The present analysis is based on data collected with the H1 detector during the 1994 running period of the HERA collider, where 27.5 GeV positrons collided with 820 GeV protons, at a CM energy of 300 GeV. A detailed description of the detector and its trigger capabilities can be found elsewhere [12].

2.1 Detector Description

Charged particles are measured by two cylindrical jet drift chambers [13, 14], mounted concentrically around the beamline inside a homogeneous magnetic field of 1.15 Tesla, yielding particle charge and momentum from the track curvature in the polar angular range² of 20° to 160°. Two double layers of cylindrical multiwire proportional chambers (MWPC) [15] with pad readout for triggering purposes are positioned inside and in between the two drift chambers, respectively. The tracking detector is surrounded by a fine grained liquid argon calorimeter [16], consisting of an electromagnetic section with lead absorbers and a hadronic section with steel absorbers. It covers polar angles between 4° and 155°. The luminosity is determined from the rate of *Bethe-Heitler* $ep \rightarrow e\gamma$ bremsstrahlung events. The luminosity system consists of an electron detector and a photon detector, located 33 m and 103 m from the interaction point in the positron beam direction, respectively. The electron detector is used to tag photoproduction events by detecting positrons scattered at small angles. A time-of-flight system (TOF) is located in the backward direction at $z \approx -2 \text{ m}$.

¹ Henceforth, charge conjugate states are always implicitly included.

² H1 is using a right-handed coordinate system with the z axis pointing in the direction of the proton beam (forward), the x axis pointing towards the centre of the storage ring. The direction of the incoming positron beam is termed backward. The polar angle θ is measured with respect to the proton direction.

2.2 Data selection and D^{*+} reconstruction

The analysis is carried out independently for the case where the scattered positron is detected in the electron tagger and for the case where it is not required to be seen. Henceforth, the respective data samples will be referred to as *tagged* and *untagged* sample. They correspond to integrated luminosities of $(2.77 \pm 0.04) \text{ pb}^{-1}$ and $(1.29 \pm 0.02) \text{ pb}^{-1}$, respectively. About 20% of the reconstructed D^* candidates in the tagged sample are also present in the untagged sample.

Proton beam induced background is reduced by requiring the event vertex to lie within $\pm 40 \text{ cm}$ of the nominal interaction point along the beam direction. A further reduction is achieved by excluding events with energy flow only into the forward region of the detector.

For each event all possible $M(K^-\pi^+)$ mass combinations are calculated with tracks of transverse momenta $p_t > 0.5 \text{ GeV}/c$. No particle identification is applied; each particle is assumed to be a kaon or a pion in turn. Pairs with an invariant mass within $\pm 80 \text{ MeV}/c^2$ of the nominal D^0 mass of $1.865 \text{ GeV}/c^2$ are combined with an additional track with $p_t > 0.15 \text{ GeV}/c$ and a charge opposite to that of the kaon candidate.

Figure 1 shows the distribution of the mass difference (3) for D^{*+} -candidates with $p_t(D^{*+}) > 2.5 \text{ GeV}/c$ and a rapidity $-1.5 < \hat{y}(D^{*+}) = -\frac{1}{2} \ln \frac{E-p_z}{E+p_z} < 1$ for the tagged and untagged samples combined. D^{*+} production is found as a distinct enhancement, containing about 190 combinations in a $\pm 2.5 \text{ MeV}/c^2$ window around the expected mass difference of $145.4 \text{ MeV}/c^2$. No enhancement is observed if the mass difference for the wrong charge combinations $M(K^-\pi^-\pi^+) - M(K^-\pi^-)$ is used instead, as shown by the shaded histogram in figure 1. The number of D^* candidates is obtained from a simultaneous fit to signal and background events in the right-sign (RS) and wrong-sign (WS) distributions of the ΔM spectra. The signal is described by a Gaussian and the background shape is parametrized by a function of the form $a_i \cdot (\Delta M - m_\pi)^b$, ($i=\text{RS, WS}$). The position and the width of the signal are determined from a fit to a larger data sample using additional trigger conditions, and then kept fixed at those values ($\Delta M_0 = 145.4 \text{ MeV}/c^2$, $\sigma(\Delta M) = 1.11 \text{ MeV}/c^2$) for all subsequent fits. Uncertainties from variations of the fit procedure are accounted for in the systematic error.

A Monte Carlo simulation is used to determine the efficiency for the reconstruction, the selection cuts, and the acceptance of the detector. Hard scattering events for direct and resolved photoproduction are generated in leading order with the PYTHIA 5.7 program [17]. The generated events are fed into the H1 detector simulation program, and are subjected to the same reconstruction and analysis chain as the real data.

The tracking efficiencies have been examined in detail using data. The single track reconstruction efficiency ϵ_{track} is obtained by scanning tracks of high p_t cosmic muons, where the measured p_t of the incident track segment is compared with that of the outgoing track segment. The p_t -dependence of ϵ_{track} is determined directly from the data by a novel method [18] based on the decay property of the pseudoscalar K_s^0 meson, decaying isotropically in its rest frame. The efficiency is found to rise from 0 to the maximum value between $p_t = 90 \text{ MeV}/c$ and $p_t = 120 \text{ MeV}/c$, and to remain constant beyond that. The precision measured in these studies is quoted as the systematic error. For single tracks the uncertainty found is $\pm 2\%$ for the track reconstruction and ${}^{+0}_{-3}\%$ for associating the track to the primary vertex. Combining them for the three tracks yields a systematic error of ${}^{+6}_{-11}\%$ on the tracking efficiency.

2.3 Analysis of electron tagged data

Tagged events are required to have a positron candidate with energy $E_{e'} > 4$ GeV in the electron tagger and to have less than 2 GeV energy deposited in the photon detector. In addition, at least one charged track candidate has to be detected by means of a MWPC trigger [15, 19] and a drift chamber track trigger [20], thus ensuring activity in the central detector. The trigger efficiency is determined from the data itself, using independent triggers. The analysis is restricted to the kinematical region $0.28 < y = 1 - E_{e'}/E_e < 0.65$ and $Q^2 < 10^{-2}$ GeV², where the acceptance of the electron tagger is above 20 % with an average value of about 60 %. As a consequence, the γp CM energy range is limited to $159 \text{ GeV} < W_{\gamma p} < 242 \text{ GeV}$, with a mean of $W_{\gamma p} \approx 200 \text{ GeV}$ and an average $\langle Q^2 \rangle \approx 10^{-3}$ GeV². The efficiency excluding the y dependent electron tagger acceptance is found to be $(48 \pm 4)\%$ and $(58 \pm 5)\%$ for direct and resolved processes, respectively.

2.4 Analysis of untagged data

The untagged sample covers the kinematical region $0.1 < y < 0.8$ and $Q^2 < 4 \text{ GeV}^2$ at an average $\langle Q^2 \rangle \approx 0.2 \text{ GeV}^2$. Contributions from DIS with $Q^2 > 4 \text{ GeV}^2$ are rejected by requiring that *no* scattered positron candidate with $E_{e'} > 10 \text{ GeV}$ be measured in the main detector. The remaining background from DIS events is suppressed by requiring $y < 0.8$ and is estimated to be less than 1 %. Here y is calculated from all measured final state particles using the Jacquet-Blondel method [21].

The events are triggered by a combination of signals from the central and rear parts of the detector. At least one MWPC track candidate is required to point backwards into the region $110^\circ < \theta < 155^\circ$. The backward TOF system must positively identify the event as a genuine ep collision by registration of a particle within the proper interaction time window and within its angular acceptance of approximately $160^\circ < \theta < 177^\circ$. The trigger efficiency for the central MWPC and drift chamber trigger components is determined by simulation to be $(84 \pm 4)\%$. For the backward part it is obtained from data, imposing the same selection criteria but using independent triggers based on local coincidences of MWPC tracks and low threshold ($> 1.5 \text{ GeV}$) signals in the liquid-argon (LAr) calorimeter [22]. Sufficient statistical precision to determine the efficiency in bins of p_t and \hat{y} is achieved by including the sideband region of the mass difference signal, $0.15 \text{ GeV}/c^2 < \Delta M < 0.18 \text{ GeV}/c^2$, and the wrong sign combinations. To account for the different event topology of the combinatorial background the efficiency is determined and parametrized as a function of y and then folded with the y spectrum of simulated D^* events. This yields efficiencies of the backward trigger component of $(28 \pm 4)\%$ for direct and $(35 \pm 5)\%$ for resolved production processes, respectively.

3 Results

The visible production cross section in ep collisions is calculated from the observed number of $D^{*\pm}$ mesons, N , in the kinematical ranges of $p_t(D^*) > 2.5 \text{ GeV}/c$ and rapidity $-1.5 < \hat{y}(D^*) < 1$ according to the formula

$$\sigma_{D^{*\pm}} = \sigma(ep \rightarrow D^{*\pm}X) = \sigma(ep \rightarrow D^{*+}X) + \sigma(ep \rightarrow D^{*-}X) = \frac{N}{L \cdot B \cdot \epsilon}, \quad (4)$$

where L denotes the integrated luminosity, ϵ the total efficiency, and $B = B(D^{*+} \rightarrow D^0\pi^+) \cdot B(D^0 \rightarrow K^-\pi^+) = 0.0273 \pm 0.0011$ [23] is the combined branching fractions of D^{*+} and D^0 mesons. For the analysis of the tagged sample, the acceptance of the electron tagger and its trigger efficiency are accounted for on an event-by-event basis. For the relative ratio of direct to resolved photoproduction processes the values predicted by the NLO QCD calculation are used (*i.e.* 79:21 for the full (\hat{y}, p_t) range or 93:7 for the visible kinematical range). The charm quark mass is assumed to be $m_c = 1.5 \text{ GeV}/c^2$, the ratios of the factorization scale for the photon, the factorization scale for the proton, and the renormalization scale are taken to be $2m_c, 2m_c$, and m_c , as recommended by the authors [5].

3.1 Visible cross section σ_{ep}

In the tagged sample the fitted number of D^* mesons, 119 ± 16 , is corrected for the electron tagger acceptance [24], yielding $N = 197 \pm 28$. For the kinematical region $p_t(D^*) > 2.5 \text{ GeV}/c^2$, $-1.5 < \hat{y}(D^*) < 1$, $Q^2 < 0.01 \text{ GeV}^2$, and $159 < W_{\gamma p} < 242 \text{ GeV}$ the *visible* ep production cross section is determined to be

$$\sigma(ep \rightarrow D^{*\pm}X) = (4.90 \pm 0.70_{-0.59}^{+0.74}) \text{ nb} \quad (\text{tagged}), \quad (5)$$

where the errors refer to the statistical and the experimental systematic error (see below).

In the case of untagged events, the fitted number of D^* mesons is 97 ± 15 events and the average total efficiency for $95 < W_{\gamma p} < 268 \text{ GeV}$ and $Q^2 < 4 \text{ GeV}^2$ is found to be 0.14 ± 0.03 . The ep cross section in the kinematical region $p_t(D^*) > 2.5 \text{ GeV}/c^2$, $-1.5 < \hat{y}(D^*) < 1$ is thus measured as

$$\sigma(ep \rightarrow D^{*\pm}X) = (20.2 \pm 3.3_{-3.6}^{+4.0}) \text{ nb} \quad (\text{untagged}). \quad (6)$$

The visible cross section is almost insensitive to both the choice of parton density parametrizations and to the mixture of direct and resolved photoproduction processes, because the efficiencies are very similar and there is no acceptance correction involved.

The experimental systematic uncertainties are listed in table 1. In the analysis of tagged data, the largest contribution (11 %) is due to the uncertainty in the track reconstruction, whereas in the untagged case the largest error arises from a 14 % uncertainty in the determination of the trigger efficiency. Adding the various uncertainties in quadrature results in a total experimental systematic error for the tagged sample of $_{-12}^{+15}\%$ for the inclusive D^* cross section and $_{-13}^{+16}\%$ for the charm cross section (see below), respectively. For the untagged sample the corresponding uncertainties are $_{-18}^{+20}\%$ and $_{-19}^{+21}\%$.

Predictions by the NLO QCD calculation for the visible cross section $\sigma_{D^{*\pm}}$ in the tagged case assuming the following pairs of proton and photon parton densities of (GRV HO[25] + GRV-G HO[25]), (MRSA'[26] + GRV-G HO), (MRSD0'[27] + GRV-G HO) and (MRSA' + LAC1[28]) yield values of 3.2, 2.8, 2.4 and 2.8 nb respectively. With the present accuracy a clear distinction is not possible, albeit a slightly better agreement is reached for parton densities with a rising gluon density distribution at low x_g . A similar conclusion results from the analysis of the untagged data. This is in agreement with measurements of the gluon density by other methods [29], *e.g.* from scaling violations of F_2 in DIS.

	Tagged	Untagged
Track trigger	5 %	5 %
Electron tagger acceptance	5 %	—
Backward trigger	—	14 %
Track reconstruction	${}^{+11}_{-6}$ %	${}^{+11}_{-6}$ %
Signal extraction/background subtraction	6 %	6 %
Luminosity	1.5 %	1.5 %
D^*, D^0 branching ratios	4 %	4 %
$c \rightarrow D^*$ branching fraction	7 %	7 %
Total experimental uncertainty	${}^{+16}_{-13}$ %	${}^{+21}_{-19}$ %

Table 1: Experimental systematic uncertainties.

3.2 Total cross sections σ_{ep} and $\sigma_{\gamma p}$

The visible cross sections (within a limited (\hat{y}, p_t) phase space) have to be extrapolated to the full (\hat{y}, p_t) phase space to obtain the total cross sections.

The individual acceptances for the direct and resolved processes as well as their relative strength depend on the choice of the parton densities, and therefore so also does the extrapolation performed by simulation. This is illustrated in table 2, which lists values for the acceptance calculated for various parton densities of the proton and photon and for different charm quark masses, for the kinematical region of the tagged sample. The numbers for the untagged case are similar. The acceptance is defined as the fraction of D^* mesons within the quoted \hat{y} and p_t ranges with respect to the total number of produced D^* .

The derivation of the total cross sections is based on simulations using a charm quark mass of $1.5 \text{ GeV}/c^2$ and assuming the GRV LO [30] parametrizations for both the proton and photon parton densities, which are in good agreement with measured parton densities. This leads to a charm ep production cross section of $\sigma_{ep} = (941 \pm 160^{+142}_{-120}) \text{ nb}$ at $\sqrt{s} = 300 \text{ GeV}$ and $Q^2 < 0.01 \text{ GeV}^2$ for the full y -range. The effect of hadronization is included using the fragmentation fraction $B_{c \rightarrow D^{*+}} = 0.260 \pm 0.021$ [31]. The ep -cross section is converted into a γp cross section using equation (1), which yields for $Q^2 < 0.01 \text{ GeV}^2$

$$\sigma(\gamma p \rightarrow c\bar{c}X) = (13.2 \pm 2.2^{+2.1}_{-1.7} {}^{+9.9}_{-4.8}) \mu\text{b} \quad \text{at} \quad \langle W_{\gamma p} \rangle \approx 200 \text{ GeV}. \quad (7)$$

For the untagged case the result over the range of $95 \text{ GeV} < W_{\gamma p} < 268 \text{ GeV}$ becomes

$$\sigma(\gamma p \rightarrow c\bar{c}X) = (12.6 \pm 2.1^{+2.6}_{-2.4} {}^{+9.4}_{-4.4}) \mu\text{b} \quad \text{at} \quad \langle W_{\gamma p} \rangle \approx 180 \text{ GeV}. \quad (8)$$

The third error indicates the additional extrapolation uncertainty as discussed below. The larger available kinematic range in $W_{\gamma p}$ allows a division into the two regions $95 \text{ GeV} < W_{\gamma p} < 190 \text{ GeV}$ and $190 \text{ GeV} < W_{\gamma p} < 268 \text{ GeV}$, thus providing information about the energy dependence of the cross section.

The results are summarized in table 3 for both analyses and compared in figure 2 with measurements by the ZEUS collaboration (at similar $W_{\gamma p}$) [9], and previous fixed-target experiments at lower energies [3]. The inner error bars represent the statistical and

Proton parton density	Photon parton density	m_c [GeV/ c^2]	Acceptance
GRV LO [30]	—	1.2	4.8 %
GRV LO [30]	—	1.5	6.3 %
GRV LO [30]	—	1.8	10.8 %
MRSB [32]	—	1.5	6.7 %
MRSB' [26]	—	1.5	10.4 %
GRV LO [30]	GRV LO [30]	1.5	2.1 %
GRV LO [30]	LAC1 [28]	1.5	0.7 %

Table 2: Acceptance for different parton density parametrizations for the direct or resolved contributions, respectively, and for different charm quark masses, as used in the extrapolation from the visible to the total cross section.

Quantity	Tagged	Untagged	Untagged
Range in $W_{\gamma p}$ (GeV)	159 - 242	95 - 190	190 - 268
Range in Q^2 (GeV 2)	$< 10^{-2}$	< 4	< 4
D^* candidates	119 ± 16	46 ± 9	51 ± 12
$\langle \epsilon_{tot} \rangle$ (%) (direct)	29 ± 2	11 ± 1	17 ± 2
Photon flux	0.0141	0.0486	0.0155
$\sigma(ep \rightarrow D^* X)$ [y, Q^2, p_t, \hat{y}] (nb)	4.90	11.0	8.5
Errors	$\pm 0.70^{+0.74}_{-0.59}$	$\pm 2.4^{+2.2}_{-2.0}$	$\pm 2.2^{+1.7}_{-1.5}$
$\sigma(\gamma p \rightarrow c\bar{c}X)$ [y, Q^2] (μb)	13.2	9.3	20.6
Errors	$\pm 2.2^{+2.1}_{-1.7} +9.9_{-4.8}$	$\pm 2.1^{+1.9}_{-1.8} +6.9_{-3.2}$	$\pm 5.5^{+4.3}_{-3.9} +15.4_{-7.2}$

Table 3: Cross section results for tagged and untagged data samples. Errors shown are statistical, experimental systematic, and for $\sigma(\gamma p \rightarrow c\bar{c}X)$ also uncertainties due to the dependence on the parton density parametrizations.

experimental systematic errors added in quadrature. The outer set of error bars indicate the total error after adding in quadrature the extrapolation uncertainty discussed below. The cross section is rising by almost one order of magnitude as compared to the low energy measurements.

Overlaid in figure 2 are predictions by the NLO QCD calculation [5] with parton density parametrizations MRSB [32] for the proton and GRV-G HO [25] for the photon. The upper and the lower solid lines delimit the range of values expected due to a variation of the renormalization scale within $m_c/2 < \mu < 2m_c$.

Calculating $\sigma_{\gamma p}$ with other combinations of parton density parametrizations increases the measured $\sigma_{\gamma p}$ by up to 75% (in the case of MRSB and LAC1), or decreases $\sigma_{\gamma p}$ by up to 35% (in the case of MRSB' and GRV-G HO). This variation reflects the uncertainties due to the choice of parton densities, and is quoted separately as a third error in the $\sigma_{\gamma p}$ cross sections. The extrapolation uncertainty due to fragmentation models ($< 30\%$, estimated by a comparison with a cluster fragmentation as implemented in the

Herwig program [33]) and due to the choice of the charm quark mass (see table 2) is not included in the error.

If the extrapolation is based on the proton parton density parametrizations MRSG, MRSA' or MRSD0' [27], the value of $\sigma_{\gamma p}$ obtained (for the tagged sample at $W_{\gamma p} = 200$ GeV) becomes $(12.2 \pm 2.0_{-1.6}^{+2.0}) \mu\text{b}$, $(8.6 \pm 1.4_{-1.1}^{+1.4}) \mu\text{b}$ or $(7.4 \pm 1.2_{-1.0}^{+1.2}) \mu\text{b}$, which are to be compared with the QCD predictions of $9.8 \mu\text{b}$, $6.0 \mu\text{b}$ or $3.9 \mu\text{b}$, respectively. Measurement and prediction change in the same manner. Hence a total cross section measurement can presently not distinguish between the different gluon densities.

3.3 Differential distributions

Differential photoproduction cross section distributions, in the visible region where no model dependent uncertainties enter from extrapolation, are obtained by determining the acceptances and efficiencies bin-by-bin, separately for the two analyses. The distributions $1/(2B_{c \rightarrow D^{*\pm}}) \cdot d\sigma(\gamma p \rightarrow D^{*\pm} X)/d\hat{y}$ are shown in figures 3a and 4a integrated over the range $2.5 \text{ GeV}/c < p_t(D^*) < 10 \text{ GeV}/c$. The distributions $1/(2B_{c \rightarrow D^{*\pm}}) \cdot d\sigma(\gamma p \rightarrow D^{*\pm} X)/dp_t$ are presented in figures 3b and 4b for the rapidity range of $-1.5 < \hat{y} < 1$. The results from the analyses of the tagged and untagged samples are not combined because they cover different $W_{\gamma p}$ (and Q^2) ranges. Note that the largest overlap between the two samples, namely 10 D^* candidates, occurs in the bin of $0 < \hat{y} < 0.5$. The error bars represent the statistical error and, for the untagged data, the bin-by-bin systematic error due to the trigger efficiency. The other systematic errors of the overall normalization are identical to the errors quoted in table 1.

The histograms shown in figures 3 and 4 represent the absolute predictions of the QCD calculation [5] including charm quark hadronization using the Peterson fragmentation function [34] (with parameter $\epsilon = 0.06$), and containing both direct and resolved photon processes. The calculations assume the parton densities MRSG for the proton and GRV-G HO for the photon, unless stated otherwise. The histograms are averages of calculations done at three representative $W_{\gamma p}$ values, weighted by the photon flux integrated over the represented range. Good agreement within errors is observed between the shape of the measured p_t distribution and the NLO QCD calculation. The \hat{y} distributions on the other hand do not agree so well, with a possible excess of the data in the forward direction.

To demonstrate the dependence on the charm quark mass, the predictions for masses $1.2 \text{ GeV}/c^2$ and $1.8 \text{ GeV}/c^2$ are also given in figure 3 (dashed histogram). In figure 4 the influence of different proton parton density functions is illustrated by overlaying QCD predictions based on the MRSA' parametrization (dashed histogram). The effect of assuming the LAC1 photon parton density parametrization (and MRSG for the proton) is marginal (dotted histogram). Although the total charm cross section is considerably larger when using LAC1, most of the difference with respect to using for example the GRV-G HO parametrization lies in the forward region ($2 < \hat{y} < 4$) and at low p_t , outside of the visible range of this measurement.

4 Diffractive photoproduction of charm quarks

A search for D^{*+} production by diffractive processes is performed in a sample of *rapidity gap* events, in which *no* final state hadronic energy flow is detected adjacent to the proton direction. The selection of diffractive events is based on a cut in $\eta_{max} < 2$ and is described elsewhere [35]. Here η_{max} denotes the pseudorapidity of the most forward calorimetric energy deposit in excess of 400 MeV. The selection of D^* candidate events and the rejection of contributions from DIS are identical to those used in the analysis of untagged data as described above. However, because of the small signal expected, the analysis has not been restricted to a particular trigger condition, and thus comprises an integrated luminosity of 2.77 pb^{-1} .

The mass difference distribution for the selected events is shown in figure 5a, exhibiting a clear D^* signal. To substantiate the evidence for a diffractive production process, the η_{max} distribution of the D^* candidate events after background subtraction estimated from wrong charge combinations, is depicted in figure 5b. The distribution shows that most events have η_{max} values close to the maximum possible value ($\eta_{max} = 3.65$), but a clear excess of events with $\eta_{max} < 2$ is observed. The data are compared with predictions of a non-diffractive model (as implemented in the PYTHIA [17] program) and a hard diffractive model (RAPGAP [36]). The former (latter) is normalized to the number of data events at $\eta_{max} > 3$ ($\eta_{max} < 2$). The sum of both models describes the shape of the data well (solid histogram in figure 5b), while the non-diffractive model alone fails to reproduce the shape of the η_{max} distribution (hatched histogram).

A lower limit on the visible diffractive cross section for the kinematical region $Q^2 < 4 \text{ GeV}^2$, $0.1 < y < 0.8$, $p_t(D^*) > 2.5 \text{ GeV}/c$, $-1.5 < \hat{y} < 1$ and $\eta_{max} < 2$ is derived. Assuming the trigger efficiency in this range to be 1 yields a conservative limit of

$$\sigma(ep \rightarrow D^{*\pm} X) > 145 \text{ pb} \quad \text{at } 90\% \text{ C.L.} \quad (\eta_{max} < 2). \quad (9)$$

The cross section limit can be compared with the predictions of the diffractive model [36], which assumes a partonic structure of the diffractive exchange. If the diffractive exchange is dominated by a hard gluon [35] at an initial scale of $Q_0^2 \approx 4 \text{ GeV}^2$, a cross section of 780 pb is predicted. On the other hand, if a quark dominated structure is assumed, the prediction is 29 pb in this model. The measured cross section is much higher than the latter prediction. Therefore, the data clearly disfavour a quark-dominated diffractive exchange.

5 Conclusions

Charm photoproduction cross sections have been measured through the detection of $D^{*\pm}$ mesons. At an average γp CM energy of 200 GeV the result is $\sigma(\gamma p \rightarrow c\bar{c}X) = (13.2 \pm 2.2_{-1.7}^{+2.1} \pm 9.9_{-4.8}^{+9.9}) \mu\text{b}$ for $Q^2 < 0.01 \text{ GeV}^2$ with $\langle Q^2 \rangle \approx 10^{-3} \text{ GeV}^2$. For the range $Q^2 < 4 \text{ GeV}^2$ with $\langle Q^2 \rangle \approx 0.2 \text{ GeV}^2$ the values are $\sigma(\gamma p \rightarrow c\bar{c}X) = (9.3 \pm 2.1_{-1.8}^{+1.9} \pm 6.9_{-3.2}^{+6.9}) \mu\text{b}$ at $\langle W_{\gamma p} \rangle \approx 142 \text{ GeV}$, and $(20.6 \pm 5.5_{-3.9}^{+4.3} \pm 15.4_{-7.2}^{+15.4}) \mu\text{b}$ at $\langle W_{\gamma p} \rangle \approx 230 \text{ GeV}$. These values are about one order of magnitude larger than those measured at previous fixed-target photoproduction experiments. Both the $W_{\gamma p}$ dependence of the photoproduction cross section and its dependence on p_t - and to a lesser extent on \hat{y} - of the D^* meson are reasonably well described by NLO QCD calculations. A slightly better agreement is reached with a steep

gluon momentum distribution in the proton. This is in accord with measurements of the gluon density by other methods [29]. The measured visible cross sections appear to be somewhat higher than the absolute QCD predictions. Evidence for charm production is found in a subsample of events which show a distinct gap of energy flow close to the direction of the proton and which can be interpreted as photon diffractive dissociation. A quark dominated diffractive exchange is clearly disfavoured by the present measurement.

Acknowledgments

We are very grateful to the HERA machine group whose outstanding efforts have made and continue to make this experiment possible. We thank the engineers and technicians for their work in constructing and now maintaining the H1 detector, the funding agencies for financial support, the DESY technical staff for continual assistance, and the DESY directorate for the hospitality extended to the non-DESY members of the collaboration. We thank Stefano Frixione for giving advice on performing the QCD calculations.

References

- [1] A. Ali et al., Proc. of the HERA Workshop, DESY, Hamburg, Vol.1 (1988) 395;
A. Ali and D.Wyler, Proc. of the Workshop “Physics at HERA”, DESY, Hamburg, Vol.2 (1991) 667 (and references therein).
- [2] “Charm production in deep inelastic scattering at HERA”, H1 Coll., contributed paper EPS-0785 to the Int. Europhysics Conference on High Energy Physics, Brussels, 1995.
- [3] M.S.Atiya et al. (CIF Coll.), Phys.Rev.Lett. 43 (1979) 414;
A.R. Clark et al. (BFP Coll.), Phys.Rev.Lett. 45 (1980) 682;
K. Abe et al. (SLAC HFP Coll.), Phys.Rev. D30 (1984) 1;
M. Arneodo et al. (EMC Coll.), Z.Phys. C35 (1987) 1;
J.J. Aubert et al. (EMC Coll.), Nucl.Phys. B213 (1983) 31; Phys.Lett. B167 (1986) 127;
M. Adamovich et al. (PEC Coll.), Phys.Lett. B187 (1987) 437;
J.C. Anjos et al. (E691 Coll.), Phys.Rev.Lett. 65 (1990) 2503;
D. Aston et al. (WA4 Coll.), Phys.Lett. B94 (1980) 113.
- [4] C.F. Weizsäcker, Z.Phys. 88 (1934) 612;
E.J. Williams, Phys.Rev. 45 (1934) 729.
- [5] S. Frixione et al., Phys.Lett. B348 (1995) 633; Nucl.Phys. B454 (1995) 3.
- [6] R.K. Ellis and P. Nason, Nucl.Phys. B312 (1989) 551;
P. Nason, S. Dawson, and R.K. Ellis, Nucl.Phys. B303 (1988) 607;
J. Smith and W.L. Van Neerven, Nucl.Phys. B374 (1992) 36.
- [7] S. Frixione et al., Nucl.Phys. B412 (1994) 225; Nucl.Phys. B431 (1994) 453.
- [8] S.J. Brodsky, P. Hoyer, C. Peterson, and N. Sakai, Phys.Lett. 93B (1980) 451;
S.J. Brodsky, C. Peterson, and N. Sakai, Phys.Rev. D23 (1981) 2745;
G.A. Schuler, Nucl.Phys. B299 (1988) 21;
G. Ingelman, L. Jönsson, and M. Nyberg, DESY 92-178 (1992).

- [9] M. Derrick et al. (ZEUS Coll.), Phys.Lett. B349 (1995) 225.
- [10] G. Feldmann et al., Phys. Rev. Lett. 38 (1977) 1313.
- [11] R. A. Eichler and Z. Kunszt, Nucl. Phys. B308 (1988) 791.
- [12] I. Abt et al. (H1 Coll.), “The H1 Detector at HERA,” DESY 93-103 (1993).
- [13] J. Bürger et al., Nucl.Instr.Meth. A279 (1989) 217.
- [14] I. Abt et al. (H1 Coll.), Phys.Lett. B328 (1994) 176.
- [15] K. Müller et al., Nucl.Instr.Meth. A312 (1992) 457.
- [16] B. Andrieu et al., Nucl.Instr.Meth. A336 (1993) 460.
- [17] T. Sjöstrand, CERN-TH-6488 (1992), Comp.Phys.Comm. 82 (1994) 74.
- [18] W. Erdmann, Dissertation, ETHZ Zürich, No. 11441, 1996, unpublished.
- [19] S. Eichenberger et al., Nucl.Instr.Meth. A323 (1992) 532.
- [20] T. Wolff et al., Nucl.Instr.Meth. A323 (1992) 537.
- [21] A. Blondel and F. Jacquet, Proceedings of the Study of an *ep* Facility for Europe, ed. U. Amaldi, DESY 79-48 (1979) 391.
- [22] D. Müller, Diploma Thesis, University Zürich, 1994, unpublished.
- [23] Particle Data Group, M. Aguilar-Benitez et al., Phys. Rev. D50 (1994) 1173.
- [24] T. Ahmed et al. (H1 Coll.), Z.Phys. C66 (1995) 529; Z.Phys. C69 (1995) 27.
- [25] M. Glück, E. Reya, and A. Vogt, Phys.Rev. D45 (1992) 3986.
- [26] A.D. Martin, R.G. Roberts, and W.J. Stirling, RAL-94-104 (1994).
- [27] A.D. Martin, R.G. Roberts, and W.J. Stirling, Phys.Lett. B306 (1993) 145.
- [28] A. Levy, H. Abramowicz, and K. Charchula, Phys.Lett. B269 (1991) 458.
- [29] S. Aid et al. (H1 Coll.), Phys.Lett. B354 (1995) 494;
Nucl.Phys. B449 (1995) 3; DESY-96/039;
M. Derrick et al. (ZEUS Coll.), Phys.Lett. B345 (1995) 576.
- [30] M. Glück, E. Reya, and A. Vogt, Phys. Lett. B306 (1993) 391.
- [31] R. Akers et al. (OPAL Coll.), CERN PPE 94/217 (1994);
LEP Coll., CERN-PPE-96/017.
- [32] A.D. Martin, R.G. Roberts, and W.J. Stirling, RAL-94-055 (1994).
- [33] G. Marchesini et al., Comp. Phys. Comm. 67 (1992) 465.
- [34] C. Peterson, D. Schlatter, I. Schmitt, and P.M. Zerwas, Phys.Rev. D27 (1983) 105.
- [35] T. Ahmed et al. (H1 Coll.), Nucl.Phys. B435 (1995) 3; Phys.Lett. B348 (1995) 681.
- [36] H. Jung, Comp.Phys.Comm. 86 (1995) 147.

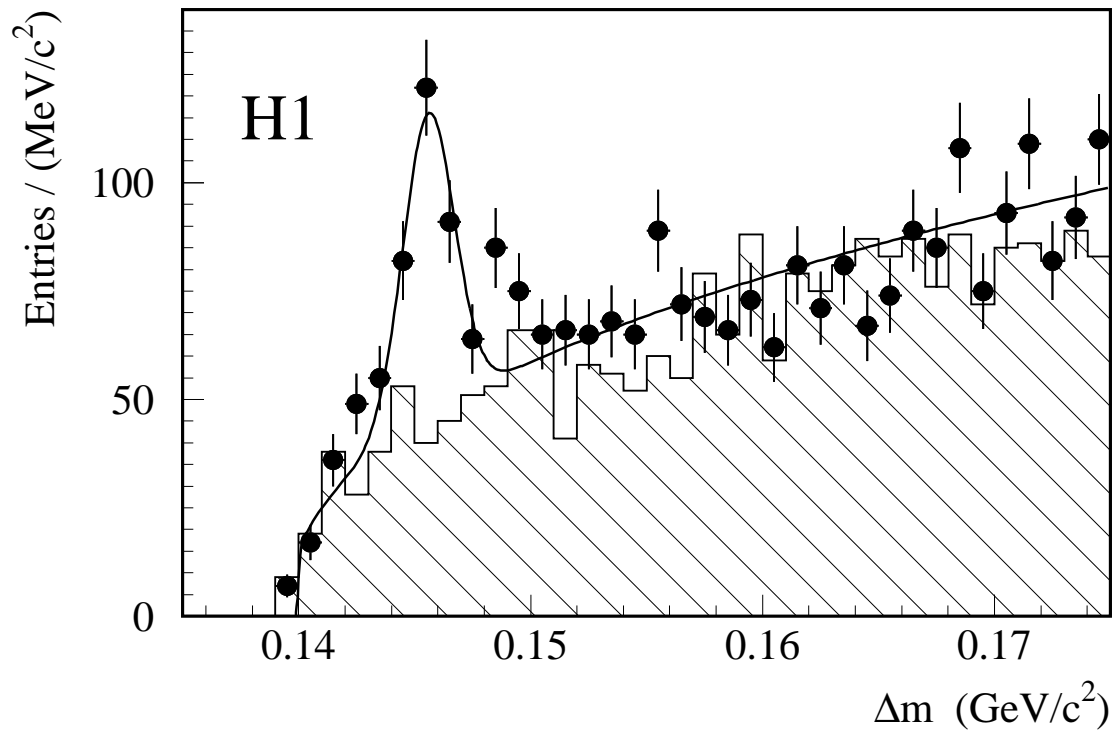


Figure 1: Distribution of the mass difference $\Delta M = M(K^-\pi^+\pi^+) - M(K^-\pi^+)$ for the combined tagged and untagged sample. The solid dots represent the data, the hatched histogram indicates the background as obtained from wrong charge combinations. The solid line is a fit of a Gaussian plus a term for the background, as described in the text, with fixed width and position of the signal.

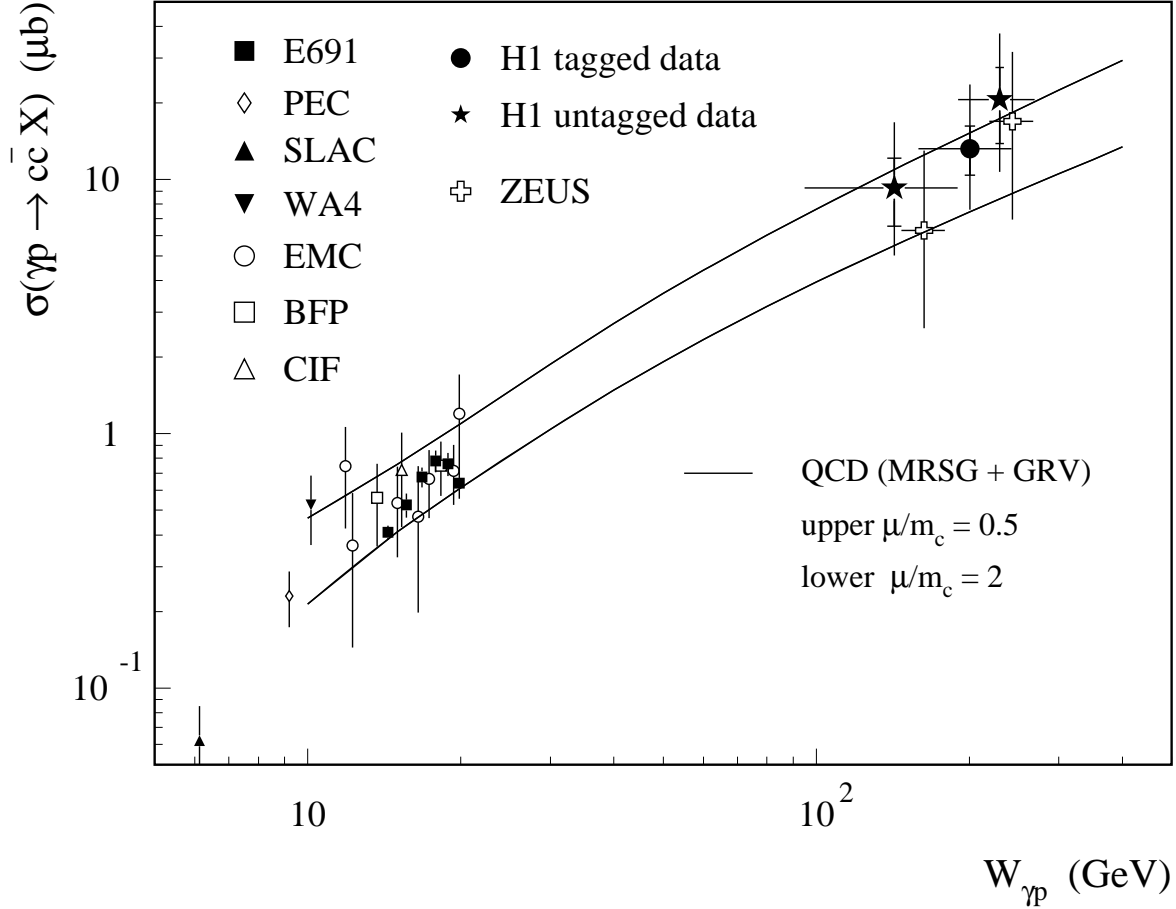


Figure 2: Total charm photoproduction cross section as a function of $W_{\gamma p}$. The solid dots and stars represent the present analyses with statistical and systematic errors added in quadrature (inner error bars). The outer error bars indicate the total error if in addition the uncertainty due to the choice of parton density parametrizations is added in quadrature. The crosses refer to the results of the ZEUS collaboration, the other symbols indicate earlier measurements at fixed-target experiments. The solid lines represent the prediction of a NLO QCD calculation using the MRSG and GRV-G HO parametrizations of the proton and photon parton densities, respectively. The upper and lower lines delimit the range of values expected from varying the renormalization scale within $0.5 < \mu/m_c < 2$.

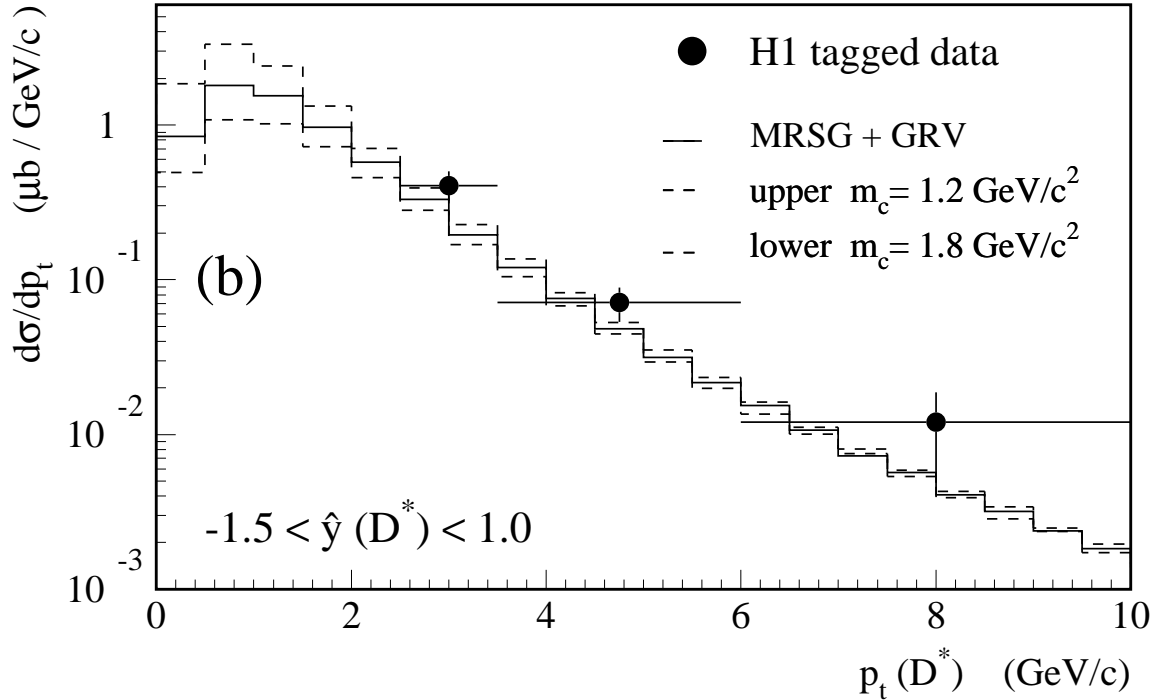
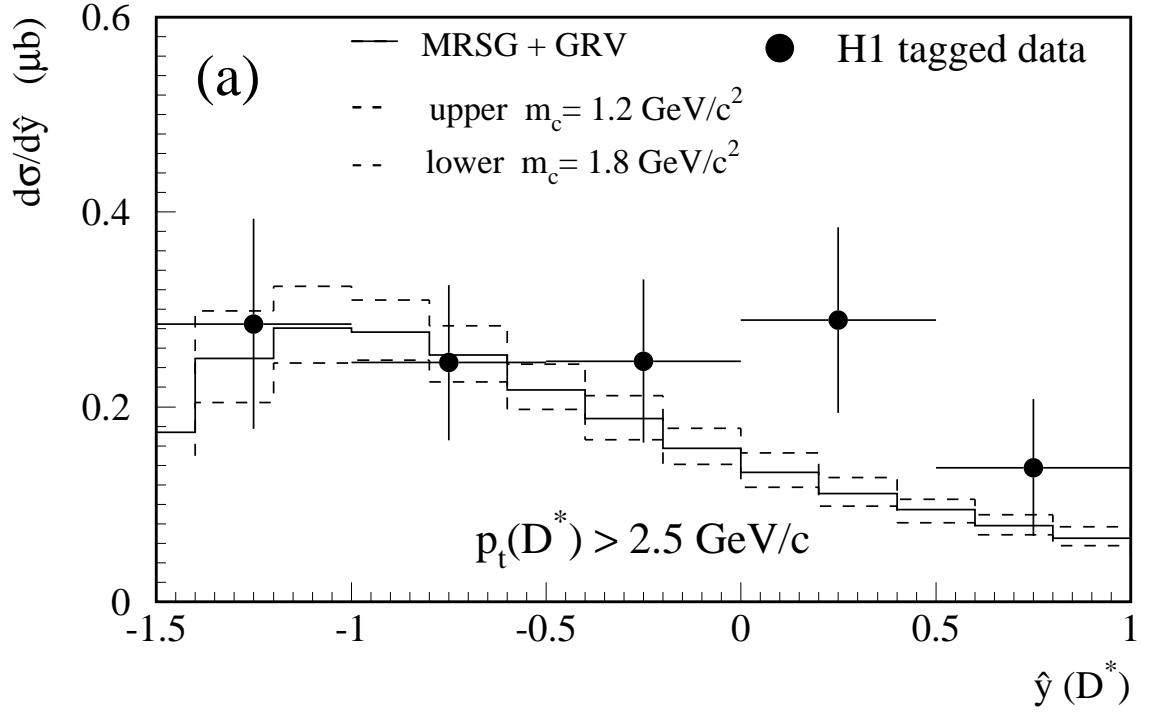


Figure 3: Differential cross sections for the tagged sample (solid dots). (a) $1/(2B_{c \rightarrow D^{*\pm}}) \cdot d\sigma(\gamma p \rightarrow D^{*\pm} X)/d\hat{y}$ for events with $p_t(D^*) > 2.5 \text{ GeV}/c$ and (b) $1/(2B_{c \rightarrow D^{*\pm}}) \cdot d\sigma(\gamma p \rightarrow D^{*\pm} X)/dp_t$ for events with $-1.5 < \hat{y}(D^*) < 1.0$. The solid histogram shows the NLO QCD prediction, using the MRSB proton parton density parametrization with a charm quark mass of $1.5 \text{ GeV}/c^2$. The upper (lower) dashed histogram indicates the effect of changing the charm quark mass to 1.2 (1.8) GeV/c^2 . The histograms are averages of calculations done at three representative $W_{\gamma p}$ values, weighted by the photon flux integrated over the represented range. Common systematic errors of $\mathcal{O}(15\%)$ are not shown.

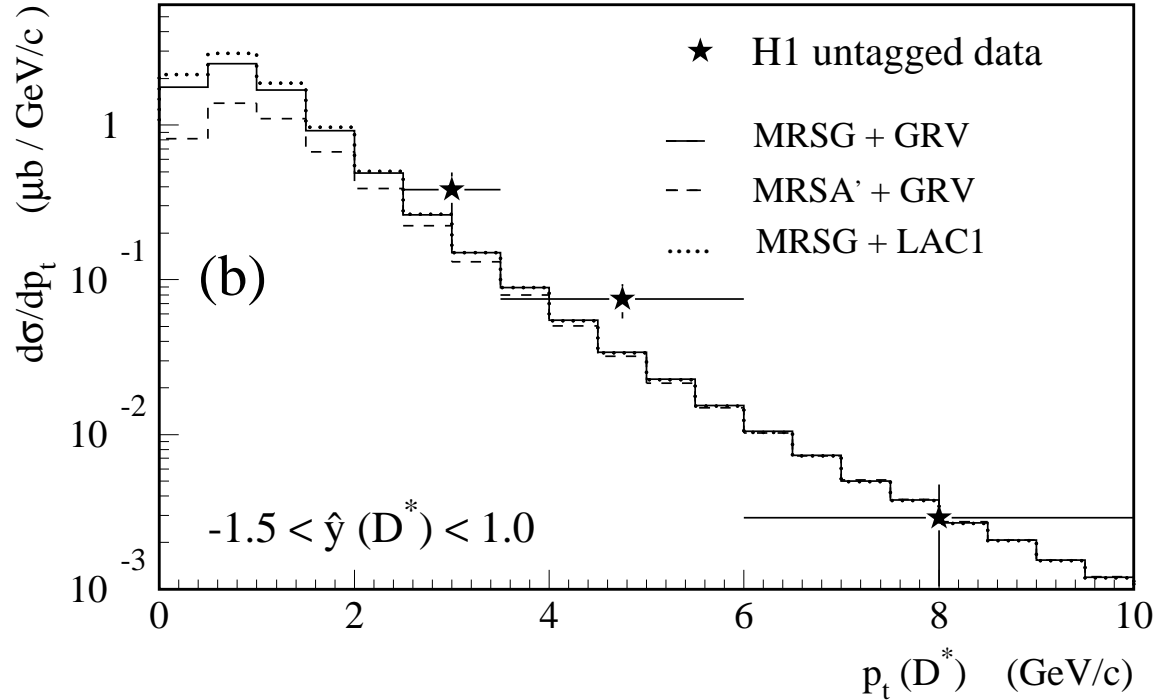
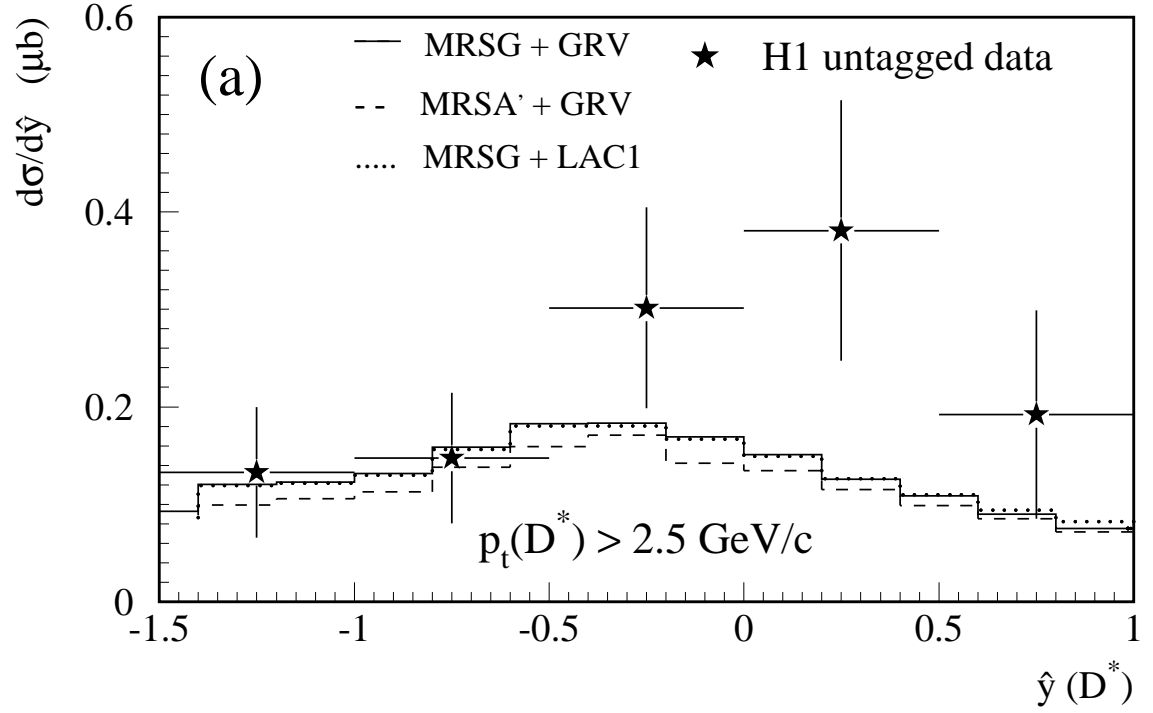


Figure 4: Differential cross sections for the untagged sample (solid stars). (a) $1/(2B_{c \rightarrow D^{*+}}) \cdot d\sigma(\gamma p \rightarrow D^{*\pm} X)/d\hat{y}$ for events with $p_t(D^*) > 2.5$ GeV/c and (b) $1/(2B_{c \rightarrow D^{*+}}) \cdot d\sigma(\gamma p \rightarrow D^{*\pm} X)/dp_t$ for events with $-1.5 < \hat{y}(D^*) < 1.0$. The histograms show NLO QCD predictions for various parton density parametrizations for the proton and the photon: MRSB + GRV-G HO (solid), MRSA' + GRV-G HO (dashed), and MRSB + LAC1 (dotted). A charm quark mass of 1.5 GeV/ c^2 is used for the calculations. The histograms are averages of calculations done at three representative $W_{\gamma p}$ values, weighted by the photon flux integrated over the represented range. Common systematic errors of $\mathcal{O}(15\%)$ are not shown.

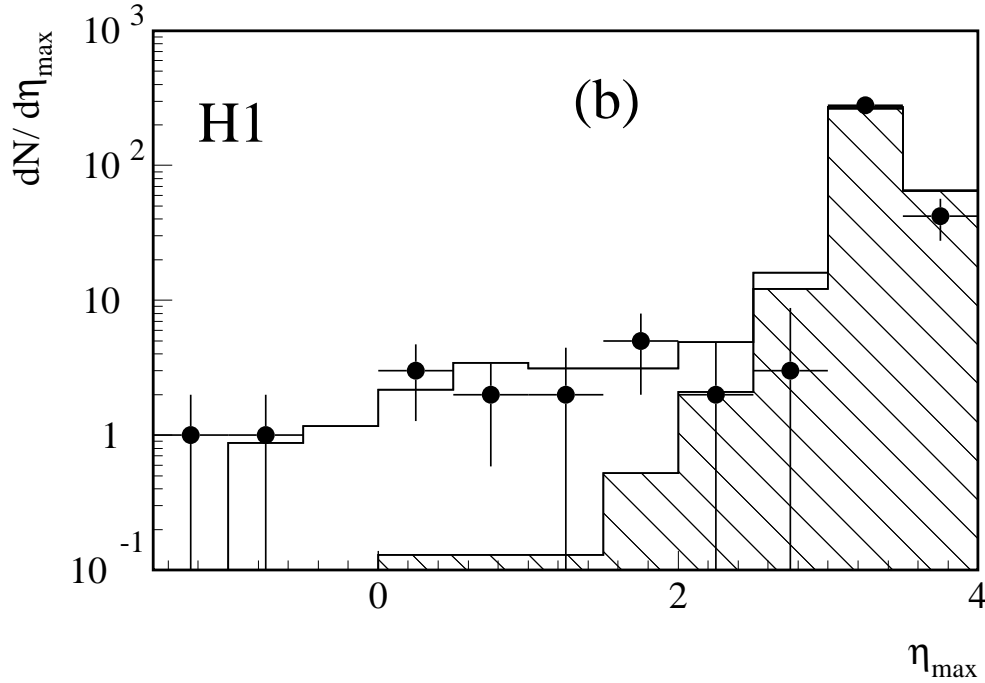
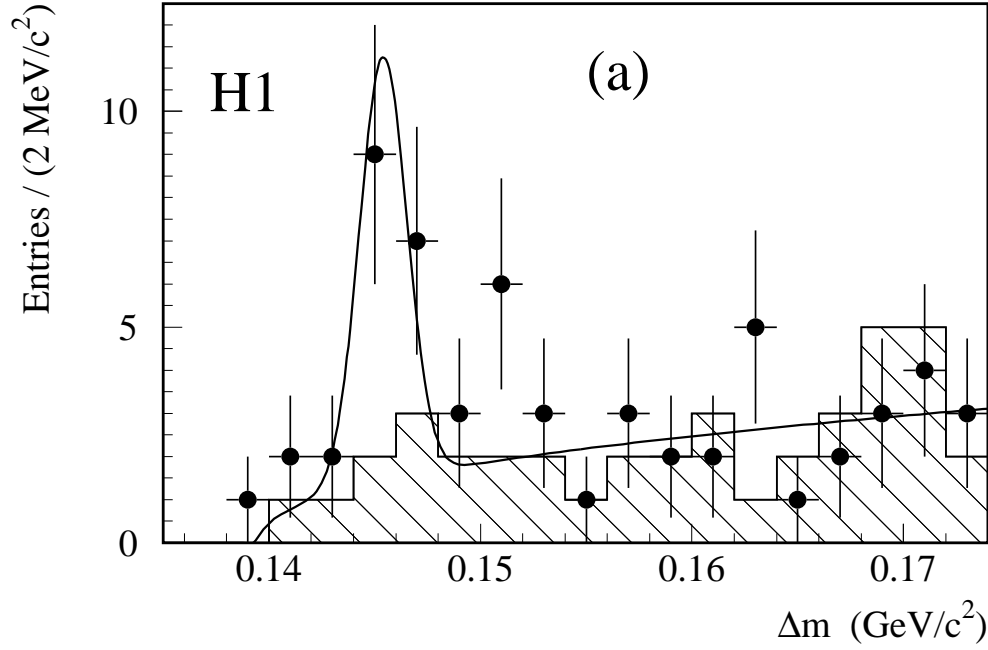


Figure 5: (a) Distribution of the mass difference $\Delta M = M(K^-\pi^+\pi^+) - M(K^-\pi^+)$ for events with a rapidity gap with $\eta_{max} < 2$. The solid dots represent the data, the hatched histogram indicates the background as obtained from wrong charge combinations. The solid line is a fit of a Gaussian function for the signal plus a background term. (b) η_{max} distribution of D^* candidate events. The hatched histogram shows the prediction of a non-diffractive model (PYTHIA), the solid histogram the sum of the non-diffractive and a diffractive (RAPGAP) model. The former (latter) is normalized to the number of data events at $\eta_{max} > 3$ ($\eta_{max} < 2$).